PHYSICAL REVIEW RESEARCH **6**, 043317 (2024)

Gas-phase thorium molecules from laser ablation

Paul Fischer,[1,*] Jonas Stricker,[2,3] Christoph E. Düllmann,[2,3,4] Dennis Renisch,[2,3]
Lutz Schweikhard,[1] and Christian Tantardini[5,6]

[1] *Institut für Physik, Universität Greifswald, 17487 Greifswald, Germany*
[2] *PRISMA$^+$ Cluster of Excellence and Department of Chemistry, Johannes Gutenberg University Mainz, 55099 Mainz, Germany*
[3] *Helmholtz-Institut Mainz, 55099 Mainz, Germany*
[4] *GSI Helmholtzzentrum für Schwerionenforschung GmbH, 64291 Darmstadt, Germany*
[5] *Hylleraas Centre, Department of Chemistry, UiT The Arctic University of Norway, 9037 Tromsø, Norway*
[6] *Department of Materials Science and NanoEngineering, Rice University, Houston, Texas 77005, USA*

(Received 14 June 2024; accepted 2 December 2024; published 26 December 2024)

Laser ablation is performed on an oxidized, roughly 35-year-old ^{232}Th foil. The produced anionic and cationic molecules are investigated utilizing precision mass measurements by a multireflection time-of-flight mass spectrometer. Molecules with up to three thorium atoms are identified. This includes oxides $\mathrm{Th}_n\mathrm{O}_x^+$ containing up to $2n-1$ oxygen atoms and further species incorporating carbon or nitrogen. In addition, signals of U^+, UO^+, and the compound species ThUO_2^+ are found. Photoexcitation reveals selected molecules' dissociation patterns. The experimental findings are compared to density functional theory calculations.

DOI: 10.1103/PhysRevResearch.6.043317

I. INTRODUCTION

Radioactive molecular beams have recently gained popularity due to their interdisciplinary positioning between atomic, molecular, and nuclear physics [1–4]. Molecules containing heavy, radioactive isotopes, such as those of the actinides, offer unique research opportunities, e.g., for the ongoing search of strong charge conjugation (C) and parity (P) violation [5–8] or the electronic dipole moment of the electron [9]. Molecular formation in hot-cavity targets and radio-frequency quadrupole cooler bunchers is of interest at radioactive ion beam (RIB) facilities [10–12].

The primordial nuclide ^{232}Th, which undergoes α decay with a half-life of 1.4×10^{10} years, is one of the few actinide species readily available in macroscopic quantities without the need for RIB facilities. It stands to reason that the gas-phase chemistry of thorium (as well as uranium) is subject to frequent investigation [13–17], not least because it requires significantly less radiation protection efforts than the more highly radioactive elements of the actinide series [18]. Interest also stems from the continuous quest for a nuclear clock that could be realized through the low-energy isomeric state of the ^{229}Th isotope [19–22]. Molecules containing this isotope are predicted to be ideal laboratories to test CP-violation theories and to search for axions [23]. However, high-resolution mass spectrometry studies on larger thorium molecules are scarce, as are those involving gas-phase anions.

Here, anionic and cationic thorium-based molecules are produced by laser ablation of a thorium target at an offline setup. The target is a 89-μm-thick foil that has been produced in the United States before it came to CERN in Geneva, Switzerland, in 1987. Part of it was sent to the University of Mainz, Germany, a year later. It oxidized due to aging. A strip of roughly 10×20 mm has now been investigated at the University of Greifswald. Due to the oxidization of the foil as well as the presence of other contaminants, a number of molecular species are identified by precision mass measurements using a multireflection time-of-flight (MR-ToF) mass spectrometer. In addition, photoexcitation is performed to determine fragmentation pathways of selected molecules with sufficient production yields. The findings are compared with results obtained from density functional theory (DFT) calculations.

II. EXPERIMENTAL SETUP AND PROCEDURE

A. Overview

The setup (Fig. 1) consists of a multireflection time-of-flight analyzer accepting ions from either a laser-ablation or magnetron sputter source. Only the former is employed in this study. Ablation is facilitated by nanosecond pulses from a Litron TRLi DPSS 170-100 operated at 532 nm and 10 Hz repetition rate. The diameter of the laser spot on the target is roughly 2 mm. For the present measurements, the pulse energy is varied between approximately 0.5 and 2 mJ depending on desired production rates. The ablation target, a 10 mm × 20 mm × 89 μm piece of thorium foil (Fig. 2), is fixed to a holder with silver-based, vacuum-grade adhesive (Acheson 1415). The black color of the foil stems from heavy oxidation, owing to its age of roughly 35 years. By moving the holder via a linear-motion feedthrough, different ares of the foil can be irradiated without breaking the vacuum. The

---

[*] Contact author: paul.fischer@uni-greifswald.de

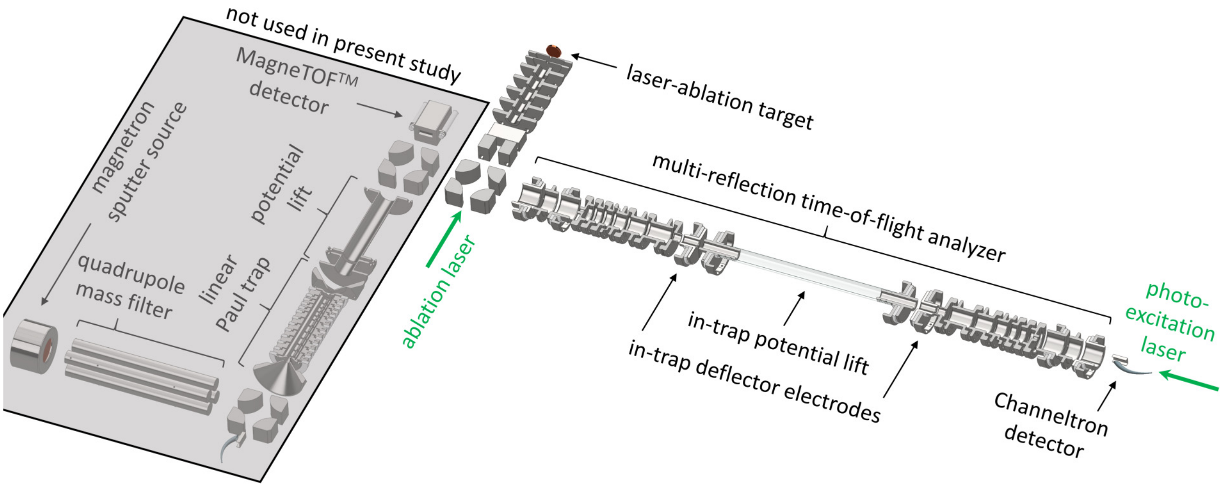

FIG. 1. Experimental setup [24] of which only the right-hand side is used in this study. The distance between components is not to scale and ion-optical components are omitted for clarity.

holder is biased to +2 kV or −2 kV to accelerate cations or anions, respectively, which are guided to the MR-ToF analyzer and subsequent channeltron detector (DeTech 402AH). Its conversion dynode allows detection of both ion polarities. In addition, the detector thus clears the optical axis and allows access for a photoexcitation laser.

Since the ions' kinetic energy is higher than all MR-ToF potentials, they traverse the analyzer and reach the downstream detector in order of ascending mass-to-charge ratio if no further measures are taken. The mass resolving power $R = t/(2\Delta t)$ of the resulting "single-path" spectrum, akin to a linear ToF mass spectrometer, is on the order of 100, where t is the ions' flight time and Δt their temporal width (full width at half-maximum) governed by, e.g., their kinetic-energy distribution.

For high-resolution, precision mass measurements, ions are captured between the opposing electrostatic mirror potentials of the analyzer by reducing their total energy with an "in-trap" potential lift [25]. The ions' flight time is greatly increased while Δt remains small due to the compensating nature of the reflecting potentials: Faster, higher-energy ions penetrate deeper into the mirror potential, incurring longer flight paths. The mass resolving power consequently rises to the order of 10^5 [26].

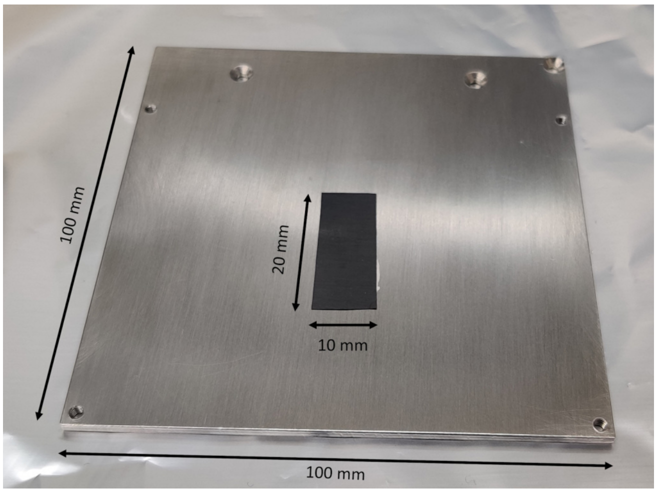

FIG. 2. Photograph of the target holder with the oxidized thorium foil. The plate is attached to a linear-motion feedthrough to allow vertical movement with respect to the ablation-laser beam.

B. MR-ToF mass measurements

The switching of the in-trap lift is synchronized to the ablation laser pulse with a delay accounting for an ion species of interest's flight from the target to the center of the analyzer. Simultaneously captured contaminants, i.e., ions of unwanted mass-to-charge values that would lap the ions of interest, are removed by switching in-trap deflector electrodes during the storage time [27]. Ions are released by reapplying the lift potential and thus reraising their energy or by lowering the exit-side mirror potential [28].

With increasing revolution number N, a species' revolution period T can be determined with greater accuracy, increasing the accuracy of its mass m calculated from a known reference via

$$m = m_{\text{ref}}\left(\frac{T}{T_{\text{ref}}}\right)^2. \tag{1}$$

Precision MR-ToF mass measurements are known to reach uncertainties down to the 10^{-8} level [29–31] and are ideally performed with isobaric references measured simultaneously to the ions of interest to minimize the influence of systematic shifts. This is, however, not a strict requirement, as Eq. (1) is viable for any pair of periods. To determine a period, a species' flight time needs to be measured for at least two different revolution numbers.

A typical measurement in this study is performed by recording the flight times of a species of interest for different revolution numbers between $N = 100$ and 1000 [Fig. 3(a)]. Since the exact capture delays and storage times are known it is sufficient to start the ToF recording with the ejection from the analyzer and measure the remaining flight time to the detector. To set the storage time matching a given revolution

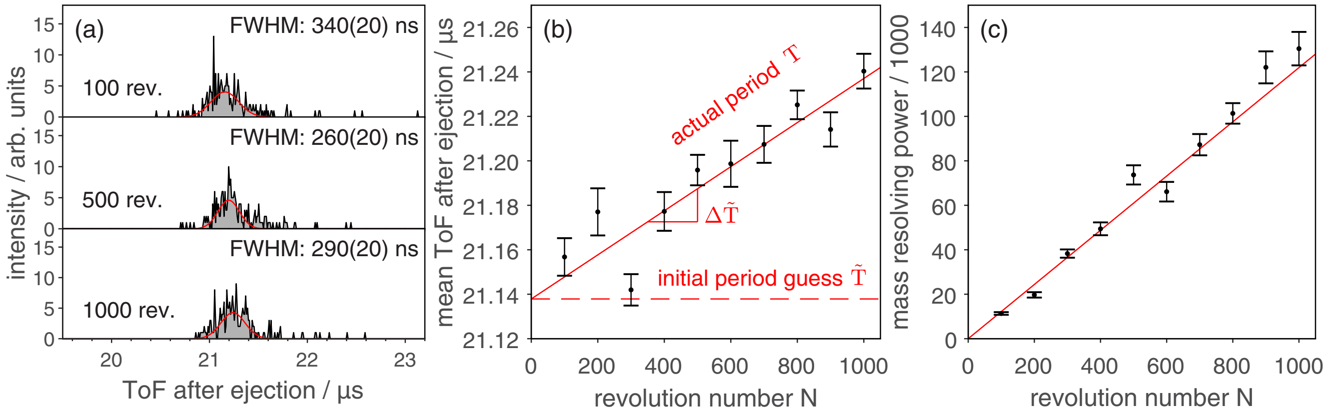

FIG. 3. (a) ToF spectra of $Th_2O_3^+$ after different revolution numbers in the MR-ToF analyzer. Flight times are recorded with respect to the ejection from the MR-ToF analyzer. Gaussian fits to the data are shown in red. (b) Mean flight times from the Gaussian fits as a function of revolution number. The dashed and solid red lines represent the initial guess for the species' period and the value resulting from a linear fit to the mean flight times, respectively. (c) Mass resolving power as a function of revolution number.

number, an initial period guess $\tilde{T}$ is required. This can either be calculated from a known reference or be roughly determined by hand. A difference between $\tilde{T}$ and the true period T leads to the recorded signals shifting in the spectra. Fitting each ToF signal with a Gaussian and the resulting mean flight times with a linear function with respect to N [Fig. 3(b)] yields an accurate estimate for T: If $\Delta\tilde{T}$ is the slope of the linear fit, i.e., the shift of the ToF signals against the assumed $\tilde{T}$ per revolution, the actual period is

$$T = \tilde{T} + \Delta\tilde{T}. \tag{2}$$

Since $\tilde{T}$ is an exact value, the accuracy of T is governed by how precisely $\Delta\tilde{T}$ is measured. While this only strictly requires a single small and large revolution number, the present approach of recording at multiple N values also serves to probe the selected mass number for isobaric species. Different isobaric molecules typically resolve into distinct ToF signals over the course of 1000 revolutions. Spectra at fewer N values are recorded in some cases with small production rates. The mass resolving power, shown in Fig. 3(c) for the example of $Th_2O_3^+$, rises to $R = 1.3(1)\times10^5$ for $N = 1000$.

C. Photoexcitation

Ions can be irradiated by a secondary laser (Continuum Minilite II, 532 nm, 6 ns) while isolated and stored in the MR-ToF analyzer to probe them for photodissociation and, in the case of anions, electron detachment. This technique of in-trap photoexcitation has been previously utilized at the present setup to study cluster fragmentation [32,33]. Briefly, the species of interest is stored in the analyzer for, in the present case, 400 revolutions while all other ions are removed by the in-trap deflectors. The excitation laser pulse is timed to irradiate the ions at their turnaround point in the entry-side mirror, where their kinetic energy is close to zero.

All fragmentation on timescales below roughly 1 µs leads to the charged product species being accelerated again only after their formation. This ensures all species retain identical total energies, which would not be the case for in-flight fragmentation. While neutral fragments cannot be detected, the charged products and remaining precursor ions are ejected towards the detector. In case more resolving power is required for product analysis, ions are retained for additional postexcitation revolutions [34]. Electron-detachment fractions are calculated by comparing the product spectra to references for which the laser beam is blocked.

III. COMPUTATIONAL DETAILS

Density functional theory is employed to validate the experimental results. Spin-polarized calculations are performed during the optimization process using atomic zero-order regular approximation (ZORA) implemented within the FHI-AIMS code [35–37] to ensure systems converge towards the collinear magnetic configuration (if present) for the minimum ground state. The spin magnetic moments in the collinear case are conventionally oriented along a compound's z axis. An initial value of 0.001 μ_B is set to initialize the systems with a small magnetic moment. Starting with a nonzero magnetization value, the calculation encourages the systems to converge toward the multiplicity of spin associated with the ground state and ensures systems relax to their true magnetic configuration during the optimization.

Atomic ZORA consists of a reformulation of the kinetic operator, which is written as

$$\hat{t}_{\text{at. ZORA}}|\varphi_j\rangle = \boldsymbol{p}\cdot\frac{c^2}{2c^2 - v_{\text{at}(j)}^{\text{free}}}\cdot\boldsymbol{p}|\varphi_j\rangle \tag{3}$$

in FHI-AIMS [35]. The potential operator v is substituted by the onsite free atom potential $v_{\text{at}(j)}^{\text{free}}$ at the atomic center at(j) associated with the basis function j. Here, c is the vacuum speed of light and $\boldsymbol{p} = -i\hbar\nabla$ the linear momentum operator. This restores the missing gauge invariance of ZORA [38,39].

The Perdew-Burke-Ernzerhof (PBE) exchange-correlation functional [40] is chosen. The total energy convergence threshold is set to 10^{-5} eV and that for interatomic forces to 10^{-4} eV/Å. For each species, different starting geometries are systematically tested according to chemical intuition. An analysis of the optimized geometries' vibrational frequencies using finite differences of analytic gradients is performed to confirm stable structures and adjust their total energy by the calculated zero-point energy.

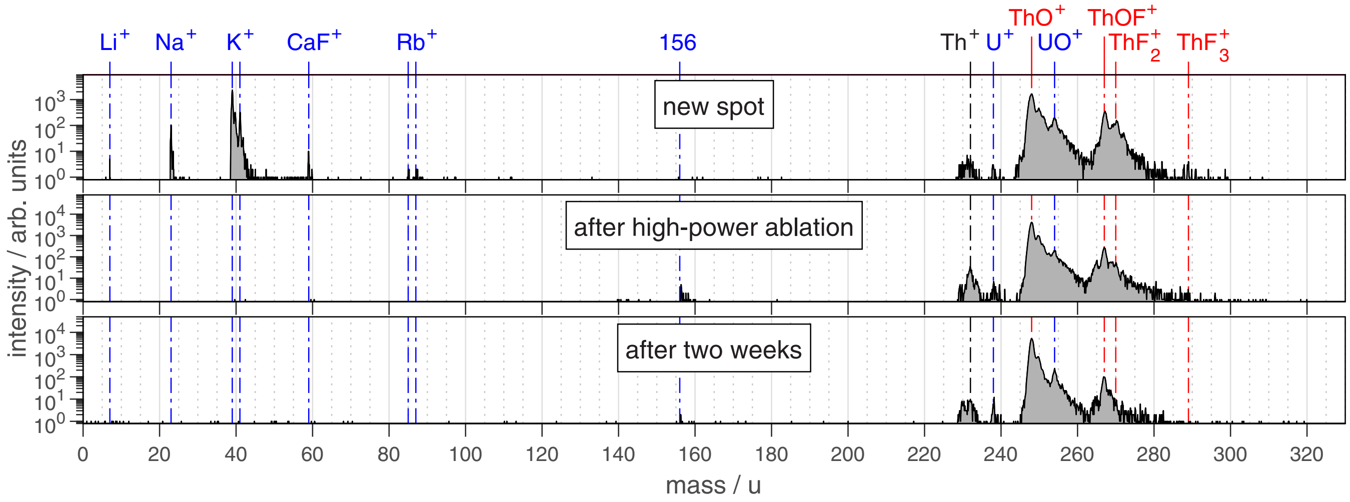

FIG. 4. Single-path spectra of cations produced from the thorium target by laser ablation. The different spectra show results for the same irradiated spot after different timescales of laser ablation. The pulse energy is 0.6 mJ for all measurements. See Table III for mass determinations. Unknown species are labeled with their mass numbers.

The FHI-AIMS basis set employs numeric atom-centered orbitals to accurately represent the electronic wave functions in all-electron density functional theory calculations. These orbitals are localized around atoms and derived by solving the Schrödinger equation for isolated atoms, allowing for precise modeling of both core and valence electrons without the use of pseudopotentials. The basis sets are structured into hierarchical "tiers," with each tier adding more orbitals for increased accuracy [35]. The tier 2 basis set is utilized in this study. Polarized and diffusive orbitals are added for each element as given in the Supplemental Material [41].

IV. RESULTS AND DISCUSSION

The production of ion species from the thorium foil is first evaluated with single-path measurements. Later on, the MR-ToF analyzer is employed to determine molecular species by precision mass measurements as outlined in Sec. II B and to record spectra with higher resolving power where needed. The results of the mass measurements are summarized in Table III in Appendix A.

A. Production and target-spot evolution in the mass range up to 300 u

Single-path spectra showing the mass range up to ≈300 u for cations and anions after different timescales of laser ablation are shown in Figs. 4 and 5, respectively. This range includes low-mass contaminants as well as molecules incorporating a single ^{232}Th atom. A "cleaning" procedure during which the spot is irradiated with high-power ablation pulses (up to ≈6 mJ in the present case) with 10-Hz repetition rate for a few hours is employed in an effort to remove contaminants as well as a possible surface layer of thorium oxide. In all measurements, the pulse energy is chosen such that no detector-saturation effects are observed on the highest signals (see figure captions for pulse-energy values). Note that the spectra are also recorded for different overall numbers of iterations to observe low-abundance signals. Thus, absolute production rates cannot be compared between the measurements. However, the evolution of relative abundances between signals reveals changing target conditions. Note that no evidence for multiply charged species is found in this study. While higher charge states have been reported for thorium ions produced by laser ablation sources [42–44] such sources operate with higher photon energies and, more crucially, significantly smaller ablation-spot diameters. It is assumed that the laser power density is not high enough in the present case for multiply charged species to be produced and extracted from the interacting plume of ablated material.

For cations (Fig. 4), expected surface contaminants like Na$^+$ and K$^+$ are present in high abundance prior to the cleaning. The amount of atomic thorium ions is negligible compared to oxygenated and fluorinated species (note the logarithmic scaling on the y axis). While the low-mass ions are virtually absent after the cleaning, thorium oxide ThO$^+$ still dominates the spectrum even after two more weeks of continuous ablation. This implies that the oxidation of the foil is more advanced than a surface layer that can be removed or that the ablation cross section of the oxide is much higher than that of Th$^+$. The formation of ThO$^+$ is known to be favored in various gas-phase reactions [13–15,45]. The abundance of fluorine-containing thorium molecules, namely, ThOF$^+$, ThF$_2^+$, and ThF$_3^+$, decreases over time compared to that of Th$^+$ and ThO$^+$ but is not removed completely.

In addition to thorium, a smaller abundance of uranium and uranium oxide is observed. A dedicated measurement is performed in which the mass range between thorium and uranium is stored for seven revolutions in the MR-ToF analyzer, increasing the mass resolving power to $R = 1000$. The isotopes ^{232}Th, ^{235}U, and ^{238}U are thus clearly separated and their ratios determined. The ratio between thorium and uranium is 6.0(7). The amount of ^{235}U$^+$ with respect to ^{238}U$^+$ is determined as 0.67(11)%, matching the natural isotopic abundance. Taking into account that uranium is observed at all times with a rather constant abundance with respect to

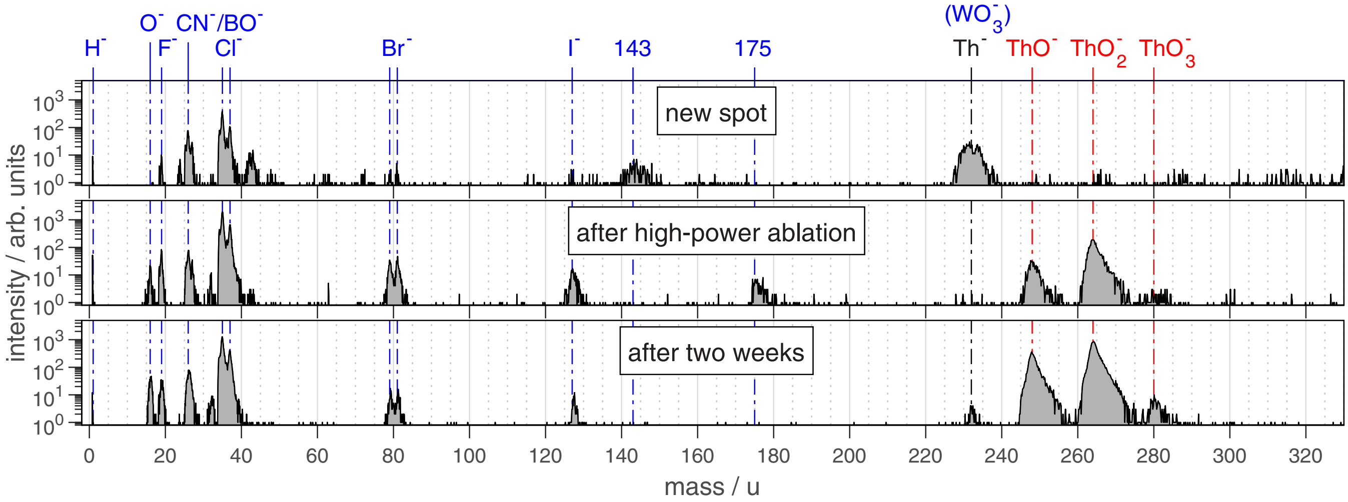

FIG. 5. Single-path spectra of anions produced from the thorium target by laser ablation. The different spectra show results for the same irradiated spot after different timescales of laser ablation. The pulse energy for each measurement is chosen to not saturate the ion detector at the largest peak: 0.5, 0.8, and 1.1 mJ.

thorium, it is suspected that the contamination most likely results from impurities of natural uranium during synthesis or refinement of the foil.

Since laser ablation is a convoluted process of bulk vaporization, ionization, and molecular formation and breakdown in the hot plume of material, determining the quantitative composition of the target from the measured spectra is nontrivial. Thus, the measured thorium-uranium ratio is not to be taken as the actual ratio of the elements in the target.

For anions, a large number of low-mass contaminants are observed even after prolonged laser ablation (Fig. 5). This includes elements not expected to naturally accumulate during storage and handling such as fluorine, bromine, and iodine. The presence of fluorine might indicate chemical processes related to the refinement of thorium [46] and is also reasonable in light of the fluorinated species found in the cationic spectra. The ratio between thorium-containing molecules and contaminant anions becomes more favorable after high-power laser ablation, with thorium mostly observed as ThO^- and ThO_2^-. In contrast, no dioxide *cation* is observed, which is likely explained by thorium's d^2s^2 electron configuration: While neutral thorium dioxide, i.e., thorium(IV) oxide, is very stable and may bind an additional electron with an electron affinity of 1.21(5) eV [47], the formation of the cation would require thorium to adopt an unfavorable +5 oxidation state. The formation of thorium monoxide ThO^+ is expected to be preferable as the ionization energy of the dioxide is somewhat higher [48]. In the anionic case, however, even the trioxide ThO_3^- is observed in small abundance, which has also been reported previously [47].

The thorium anion Th^- is only present in small abundances. Note that the top spectrum of Fig. 5 suggests a large signal at mass number $A = 232$ for the new target spot. However, precision mass analysis reveals this to be a set of four species with $A = 230, 231, 232$, and 234 identified as tungsten trioxide $^{182-184,186}W\,^{16}O_3^-$ (see Appendices A and B). The origin of these contaminants is unknown and they are fully removed by the cleaning procedure. The small signal in later spectra is confirmed to be Th^-. Note that, in contrast, no anionic uranium or uranium oxide is observed.

B. Thorium dimers and trimers

Experimental studies on gas-phase molecules containing multiple thorium atoms are scarce [16,49,50]. The present high-vacuum laser-ablation source typically only produces larger molecules in small abundance due to the high temperatures in the plume of vaporized material. While no larger anionic species are observed in this study, distributions of thorium-dimer- and thorium-trimer-based molecules are produced with higher pulse energies in the case of cations (Figs. 6 and 7). Thorium oxides $Th_nO_x^+$ are dominant in both cases (red labels), with a maximum number of $x = 2n - 1$ oxygen atoms attached. This matches the fact that only the monoxide is observed for the monomer (Fig. 4). The generalized trend might suggest that the molecules aggregate from neutral thorium(IV) oxide ThO_2 during laser ablation to form Th_nO_{2n}. For the cations, at least one oxygen atom is then removed to accommodate the positive charge, forming the most abundant $Th_nO_{2n-1}^+$ configuration.

There are also a number of species carrying different combinations of carbon, nitrogen, and oxygen (blue labels in Figs. 6 and 7). Although carbon and nitrogen are not expected to accumulate in or on the target during prolonged exposure to atmosphere, note that CN^- is present in the anionic spectra (Fig. 5) which may be supplying the atoms for molecule formation. Also note that due to the large abundances of $Th_2O_3^+$ and $Th_3O_5^+$, an additional signal matching the molecules' configuration containing a single ^{18}O isotope (0.2% natural abundance) is observed. This is confirmed by the signals at the corresponding mass values matching the expected isotopologue ratio for three and five oxygen atoms, respectively.

Note that not all species' masses are measured due to decreasing production rates in the case of the trimer. However, the composition can be inferred from the general structure of the signals. Specifically, all oxides up to $Th_3O_4^+$ are paired

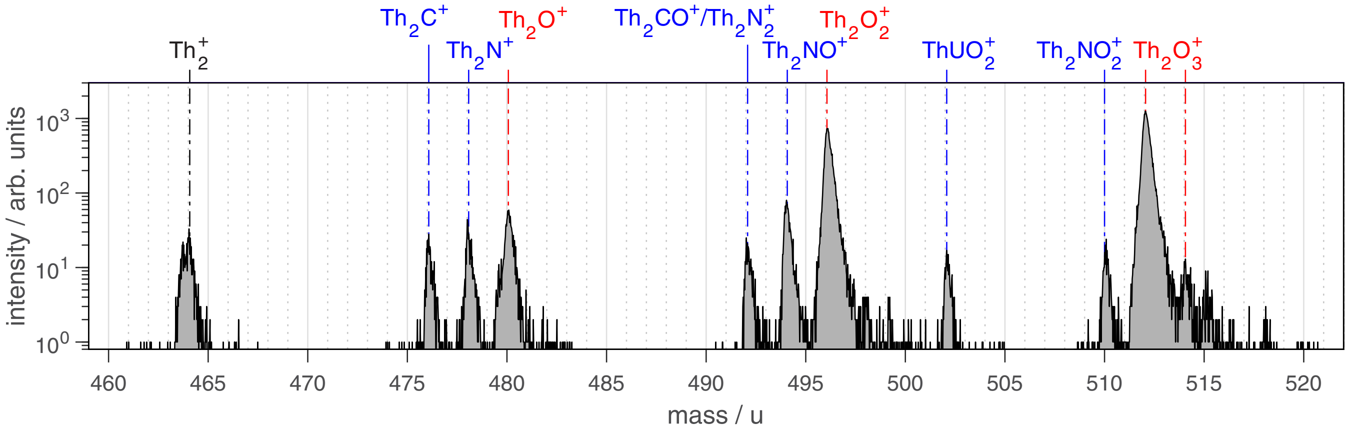

FIG. 6. Mass spectrum of thorium-dimer-based cationic species. The spectrum is recorded at 10 revolutions in the MR-ToF analyzer with 1.0-mJ ablation pulse energy. Marked species are identified by precision mass measurements (see Table III). The $Th_2O_3^+$ molecule is assigned to two signals, the heavier of which denotes the $^{16}O_2\,^{18}O$ composition.

with a species in which an oxygen atom is substituted by nitrogen or, presumably, carbon. However, the carbon-containing molecules belonging to the largest oxides $Th_2O_3^+$ and $Th_3O_5^+$, namely, $Th_2CO_2^+$ and $Th_3CO_4^+$, are absent.

An interesting finding is the species with mass number $A = 502$ identified as $ThUO_2^+$. It represents the counterpart of $Th_2O_2^+$ with one thorium atom substituted by uranium. It is the only compound oxide observed. This might be explained by the fact that both ThO^+ and UO^+ are present in the single-path spectra in some abundance (Fig. 4). The compounds might be formed in the ablation plume similar to the suspected mechanism producing the larger thorium oxides. It is unclear, however, why other possible thorium-uranium compounds are not observed.

C. Photoexcitation

Species with sufficient production rates are probed by the photoexcitation laser as outlined in Sec. II C. The results for fragmentation and electron detachment are summarized in Table I. If multiple fragments are observed for a given precursor, at least two pathways with threshold energies below the total excitation energy must be present. After the photons are absorbed through the molecules' electronic system, their energy can either lead to direct detachment or thermalize to the vibrational degrees of freedom from where it is available for dissociation based on statistical processes of intramolecular vibrational redistribution.

For the investigated anionic species, a trend is observed going from atomic Th^- to ThO_3^-: Only electron detachment is found for Th^- (trivially), ThO^-, and ThO_2^- with the cross sections reducing from virtually 100% to 63%. It reduces to 13% for the trioxide, which is the only species for which a small abundance of photofragments is observed. Excitation of the unknown anion with mass number $A = 175$ does not yield any fragments or neutralization.

Neutralization is not possible for isolated gas-phase cations. All probed monomer-based species, namely, ThO^+, UO^+, $ThOF^+$, ThF_2^+, and ThF_3^+ are found to be stable against 532-nm photoexcitation. The dimer-based species, however, show fragmentation.

The fragment spectra of the simple oxides Th_2O^+, $Th_2O_2^+$, and $Th_2O_3^+$ are shown in Fig. 8 together with that of the pure thorium dimer Th_2^+. Note that, even though the precursor

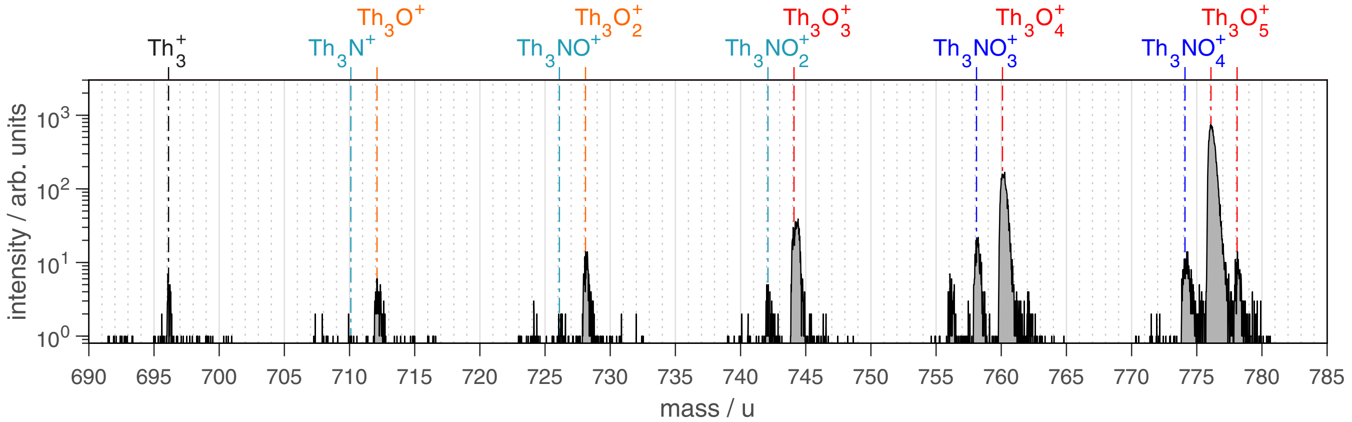

FIG. 7. Mass spectrum of thorium-trimer-based cationic species. The spectrum is recorded at 20 revolutions in the MR-ToF analyzer with 1.3-mJ ablation pulse energy. The $Th_3O_5^+$ molecule is assigned to two signals, the heavier of which denotes the $^{16}O_4\,^{18}O$ composition. Orange and light blue signals have not been confirmed by precision mass measurements.

TABLE I. Relative fragmentation and electron-detachment abundances for photoexcitation of selected ion species. Excitation is performed with 1 mJ pulse energy, 532 nm (2.33 eV), and ≈3 mm laser-beam diameter at the point of interaction.

Precursor	Total fragmentation (%)	Total detachment (%)	Fragment species [rel. abundance (%)]
Th^-	0	99.5(4)	
ThO^-	0	99.7(1)	
ThO_2^-	0	62.7(5)	
ThO_3^-	1.6(1)	12.6(6)	O^- (48(3)), ThO_2^- (52(3))
$A = 175$	0	0	
ThO^+	0		
UO^+	0		
$ThOF^+$	0		
ThF_2^+	0		
ThF_3^+	0		
Th_2^+	14(2)		Th^+ (100)
Th_2C^+	15(1)		Th^+ (74(2)), ThC^+ (26(2))
Th_2N^+	30(1)		Th^+ (77(1)), ThN^+ (23(1))
Th_2O^+	37(2)		Th^+ (60(4)), ThO^+ (40(4))
Th_2NO^+	9(1)		ThN^+ (47(6)), ThO^+ (53(6))
$Th_2O_2^+$	21(2)		ThO^+ (100)
$ThUO_2^+$	35(2)		ThO^+ (17(3)), UO^+ (83(3))
$Th_2NO_2^+$	0		—
$Th_2O_3^+$	17(3)		ThO^+ (100)

signals in the linear-ToF photoexcitation spectra are broad, precursor selection is performed with resolving powers of $R \approx 40\,000$ and species have been investigated for isobaric contaminants with up to $R \approx 100\,000$ beforehand. Smaller (charged) fragment species, e.g., atomic or molecular oxygen, are not observed. For the Th_2O^+ precursor, an additional measurement with higher postexcitation resolution [34] is also performed to exclude the possibility of Th_2^+ being produced.

The spectra of Fig. 8 show a general tendency of the studied species to form ThO^+ fragments whenever possible. Next to the trivial case of the thorium dimer, Th^+ is only found as a fragment after excitation of Th_2O^+. For that precursor, since no Th_2^+ or O^+ is observed, every fragmenting molecule splits into Th and ThO. Both fragments have a chance to retain the charge with a three-to-two branching ratio. ThO^+ breakoff is also observed for Th_2NO^+, whereas $Th_2NO_2^+$ is found stable against photofragmentation (see Table I). Analogously, ThN^+ and ThC^+ are produced from carbon- or nitrogen-containing precursors.

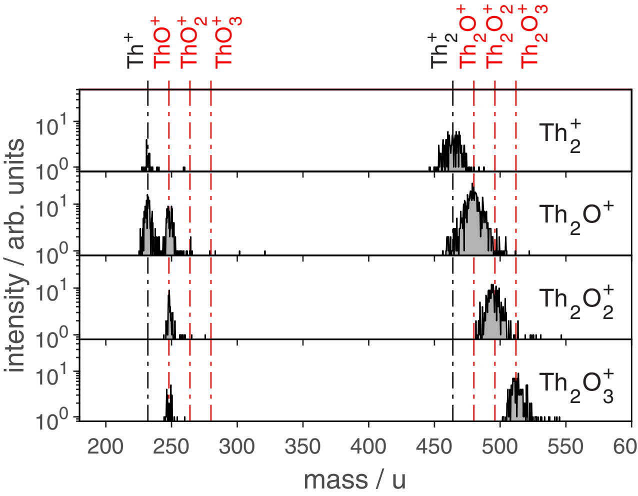

FIG. 8. Photofragment spectra for excitation of thorium-dimer oxides with 532-nm and 1-mJ pulse energy.

The compound species $ThUO_2^+$ resembles $Th_2O_2^+$ in that it fragments into ThO^+ and the analogous UO^+. The molecule splits with the uranium oxide being favored to retain the charge with a five-to-one ratio. The pulse energy of the excitation laser is varied between 0.1 and 1 mJ in an additional measurement series (Fig. 9). Both fragment abundances are well described by linear functions and their ratio is found to be constant. This suggests they result from competing pathways after single-photon absorption. The currently accepted, experimental ground-state ionization energies are 6.60 eV for ThO [51] and 6.03 eV for UO [52]. Earlier measurements yielded lower values in both cases [6.1(1) eV for ThO [48,53], 5.6(1) eV for UO [48]] which is attributed to excited states from higher temperatures. For the present high-vacuum laser ablation, such high temperatures are also expected [54]. In any case, the difference of ≈0.6 eV between the two oxides seems to be preserved, which qualitatively matches the present observation of UO^+ being more readily produced by photodissociation.

D. Computational results

Thorium is a heavy element of the actinide series, characterized by a $6d^2\,7s^2$ electronic configuration with empty f orbitals. Its status as a heavy element necessitates considering relativistic effects. The inclusion of thorium into different neutral and charged molecules also necessitates the consideration of magnetization. Thus, spin-polarized atomic ZORA calculations are performed as outlined in Sec. III. Spin-orbit coupling is not considered since its effect on the present investigation

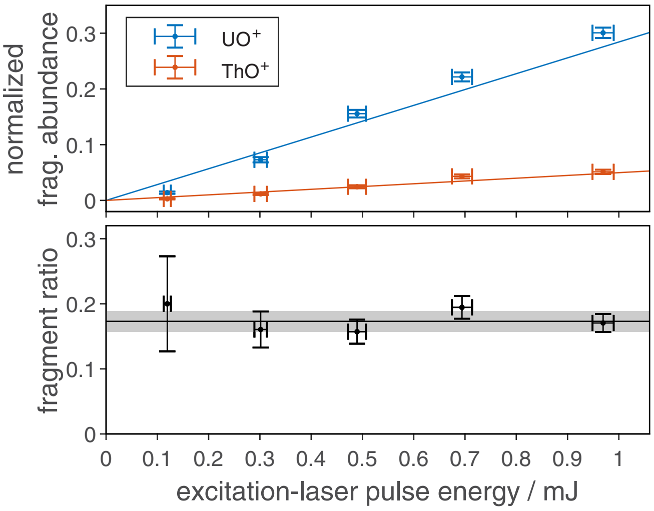

FIG. 9. Top: Fragment abundances of ThO^+ and UO^+ as a function of pulse energy for 532-nm photoexcitation of $ThUO_2^+$. Lines are linear fits to the data. The data are normalized to the total precursor signal prior to excitation. No other product species are observed. Bottom: Ratio of ThO^+ to UO^+ fragments with weighted mean and standard deviation.

TABLE II. Dissociation energies D for experimentally observed fragmentation pathways of small thorium-based molecules. All data result from DFT calculations. Relative energies of additional isomers are given in the Supplemental Material [41].

Species	D (eV)
ThO_3^-	4.61 ($O^- + ThO_2$), 7.18 ($ThO_2^- + O$)
Th_2^+	4.96 ($Th^+ + Th$)
Th_2C^+	7.68 ($ThC^+ + Th$), 7.71 ($Th^+ + ThC$)
Th_2N^+	5.64 ($Th^+ + ThN$), 6.10 ($ThN^+ + Th$)
Th_2O^+	3.88 ($Th^+ + ThO$), 4.38 ($ThO^+ + Th$)
Th_2NO^+	6.06 ($ThN^+ + ThO$), 6.10 ($ThO^+ + ThN$)
$Th_2O_2^+$	4.10 ($ThO^+ + ThO$)
$ThUO_2^+$	4.37 ($UO^+ + ThO$), 4.64 ($ThO^+ + UO$)
$Th_2O_3^+$	4.87 ($ThO^+ + ThO_2$)

of geometrical configurations was assumed to be negligible. Such effects would need to be taken into account, however, if the molecules' optical properties were to be studied.

The ground-state geometries of all photoexcitation precursors are shown in Fig. 10. The energy and coordinate data for the ground states as well as higher-energy isomers are available in the Supplemental Material [41].

The structures of the thorium-monomer species (top row of Fig. 10) are mostly simple. In contrast, more variation is possible for the dimer-based molecules. Notably, next to the trivial case of Th_2^+, the triangular Th_2C^+, Th_2N^+, and Th_2O^+ isomers could be stabilized by the presence of a thorium-thorium bond. Actinide-actinide bonds are expected to be weak [55,56]. Experimental observations are limited to a few select cases such as simple uranium and thorium dimers [49,57], crystalline clusters [58], and fullerene-encased U_2 [59].

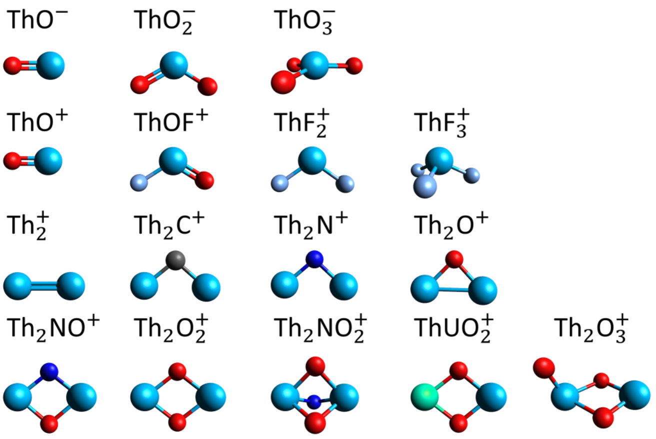

FIG. 10. Ground-state structures for investigated thorium molecules. The geometries are found using spin-polarized atomic ZORA as outlined in Sec. III. The corresponding coordinates as well as higher-energy isomeric configurations are available in the Supplemental Material [41].

In the present case, the triangular structures are thus investigated using the theory of "atoms in molecules" (AIM) [60] developed by Bader using the CRITIC2 code [61,62]. It provides a quantum mechanical framework to describe chemical bonding in molecules based on the topology of the electron density distribution. Within this theory, the fundamental concept of a "bond critical point" (BCP) describes a local minimum of the electron density at a point in space along the bond path between two nuclei. The presence of a BCP between two atoms is indicative of a bond between them and the properties of the electron density at the BCP can provide insights into the nature of the bond [63–66].

The AIM analysis reveals different characteristics for the probed systems. A Th-Th BCP is found only for Th_2O^+ with an electron density of 0.48 e/a_0^3, which is on the same order of magnitude as the Th-O BCPs with 0.92 e/a_0^3. This suggests a significant interaction between the thorium atoms. For Th_2C^+ and Th_2N^+, as well as all other observed species, carbon, nitrogen, or oxygen atoms form bridges between the thorium atoms instead. This is also found for the $ThUO_2^+$ compound species and leads to nonlinear geometries for all molecules consisting of more than three atoms.

The most remarkable structure is found for $Th_2NO_2^+$ which adopts a closed, compact geometry. Note that this species is found to be stable against photoexcitation in this study. The dimer-based structures in general match the photoexcitation results in that no Th_2^+ fragments are observed. Forming the Th_2^+ structure from the folded geometries of the larger molecules is expected to require significant reconfiguration. Dissociation into the observed ThX fragments should be more favorable.

Calculated dissociation energies D are listed in Table II for all observed fragmentation pathways. The dissociation energy is defined as the energy difference between the global minima of the precursor and the charged and neutral fragments. Comparing the results to the measured relative abundances (Table I) again reveals qualitative agreement. In the cases of Th_2N^+, Th_2O^+, and $ThUO_2^+$, the higher-abundant fragments correlate to lower dissociation energies. The relatively small energy differences of some hundreds of meV, compared to the

TABLE III. Ion species for which precision mass measurements have been performed (not exhaustive of all observed signals). The species denoted "REFERENCE" is used for calculations in their respective vertical blocks. No reasonable assignment could be performed for entries denoted by (?). Literature mass values are taken from [67].

	Cations			Anions		
A	Species	Ion mass (u) (calculated)	Ion mass (u) (AME2020)	Species	Ion mass (u) (calculated)	Ion mass (u) (AME2020)
26				${}^{12}\mathrm{C}\,{}^{14}\mathrm{N}^-$	26.0033(2)	26.0036
				${}^{10}\mathrm{B}\,{}^{16}\mathrm{O}^-$	26.0089(4)	26.0084
27				${}^{11}\mathrm{B}\,{}^{16}\mathrm{O}^-$	27.0048(2)	27.0048
35				${}^{35}\mathrm{Cl}^-$	REFERENCE	34.9694
39	${}^{39}\mathrm{K}^+$	REFERENCE	38.9632			
59	${}^{40}\mathrm{Ca}\,{}^{19}\mathrm{F}^+$	58.9613(5)	58.9604			
79				${}^{79}\mathrm{Br}^-$	78.9192(7)	78.9189
156	?	155.903(1)				
175				?	174.963(1)	
230				${}^{182}\mathrm{W}\,{}^{16}\mathrm{O}_3^-$	229.935(2)	229.933
231				${}^{183}\mathrm{W}\,{}^{16}\mathrm{O}_3^-$	230.937(2)	230.936
232	${}^{232}\mathrm{Th}^+$	232.038(2)	232.038	${}^{232}\mathrm{Th}^-$	232.037(2)	232.039
				${}^{184}\mathrm{W}\,{}^{16}\mathrm{O}_3^-$	231.936(2)	231.936
234				${}^{186}\mathrm{W}\,{}^{16}\mathrm{O}_3^-$	233.941(2)	233.940
238	${}^{238}\mathrm{U}^+$	238.049(2)	238.050			
248	${}^{232}\mathrm{Th}\,{}^{16}\mathrm{O}^+$	REFERENCE	248.032	${}^{232}\mathrm{Th}\,{}^{16}\mathrm{O}^-$	REFERENCE	248.034
251	${}^{232}\mathrm{Th}\,{}^{19}\mathrm{F}^+$	251.036(2)	251.036			
254	${}^{238}\mathrm{U}\,{}^{16}\mathrm{O}^+$	254.045(2)	254.045			
264				${}^{232}\mathrm{Th}\,{}^{16}\mathrm{O}_2^-$	264.028(2)	264.028
267	${}^{232}\mathrm{Th}{}^{16}\,\mathrm{O}\,{}^{19}\mathrm{F}^+$	267.032(2)	267.031			
270	${}^{232}\mathrm{Th}\,{}^{19}\mathrm{F}_2^+$	270.034(2)	270.034			
280				${}^{232}\mathrm{Th}\,{}^{16}\mathrm{O}_3^-$	280.022(2)	280.023
289	${}^{232}\mathrm{Th}\,{}^{19}\mathrm{F}_3^+$	289.033(2)	289.033			
464	${}^{232}\mathrm{Th}_2^+$	464.073(4)	464.076			
476	${}^{232}\mathrm{Th}_2\,{}^{12}\mathrm{C}^+$	476.076(4)	476.076			
478	${}^{232}\mathrm{Th}_2\,{}^{14}\mathrm{N}^+$	478.079(4)	478.079			
480	${}^{232}\mathrm{Th}_2\,{}^{16}\mathrm{O}^+$	480.070(4)	480.070			
492	${}^{232}\mathrm{Th}_2\,{}^{12}\mathrm{C}\,{}^{16}\mathrm{O}^+$	492.070(4)	492.070			
	${}^{232}\mathrm{Th}_2\,{}^{14}\mathrm{N}_2^+$	492.082(4)	492.082			
494	${}^{232}\mathrm{Th}_2\,{}^{14}\mathrm{N}\,{}^{16}\mathrm{O}^+$	494.075(4)	494.074			
496	${}^{232}\mathrm{Th}_2\,{}^{16}\mathrm{O}_2^+$	REFERENCE	496.065			
502	${}^{232}\mathrm{Th}\,{}^{238}\mathrm{U}\,{}^{16}\mathrm{O}_2^+$	502.075(4)	502.078			
510	${}^{232}\mathrm{Th}_2{}^{14}\,\mathrm{N}\,{}^{16}\mathrm{O}_2^+$	510.067(4)	510.068			
512	${}^{232}\mathrm{Th}_2\,{}^{16}\mathrm{O}_3^+$	512.063(4)	512.060			
514	${}^{232}\mathrm{Th}_2\,{}^{16}\mathrm{O}_2\,{}^{18}\mathrm{O}^+$	514.061(4)	514.065			
744	${}^{232}\mathrm{Th}_3\,{}^{16}\mathrm{O}_3^+$	744.100(6)	744.098			
758	${}^{232}\mathrm{Th}_3\,{}^{14}\mathrm{N}\,{}^{16}\mathrm{O}_3^+$	758.103(7)	758.101			
760	${}^{232}\mathrm{Th}_3\,{}^{16}\mathrm{O}_4^+$	760.093(6)	760.093			
774	${}^{232}\mathrm{Th}_3{}^{14}\,\mathrm{N}\,{}^{16}\mathrm{O}_4^+$	774.103(7)	774.096			
776	${}^{232}\mathrm{Th}_3\,{}^{16}\mathrm{O}_5^+$	REFERENCE	776.088			
778	${}^{232}\mathrm{Th}_3\,{}^{16}\mathrm{O}_4\,{}^{18}\mathrm{O}^+$	778.088(7)	778.092			

photon energy of 2.33 eV, also explain why both pathways are observed. However, for $\mathrm{Th_2C^+}$, the calculated energies are virtually identical while a 75:25 abundance difference is measured. This mismatch cannot be explained from the present experimental or computational data set. In the cases of $\mathrm{Th_2NO^+}$ and $\mathrm{Th_2O_3^-}$ the measured abundances of the charged products show a 50:50 ratio although the dissociation energies differ. Note that no reaction barriers are considered in the calculations. Also note that the detachment abundance is significantly larger than the very small total fragment abundance in the case of $\mathrm{Th_2O_3^-}$. Sequential pathways including electron detachment might lead to the mismatch of the experimental and calculated results for the anionic precursor.

The absolute values of the calculated dissociation energies are in the range of two- or three-photon absorption for the present laser wavelength. In general, this is possible but it contradicts the experimental findings in the case of $\mathrm{ThUO_2^+}$ (see Fig. 9), where evidence points to single-photon dissociation. As already stated above, high temperatures and, thus, high rovibrational energies prior to photoexcitation are expected for molecules produced by the present source. It is unclear, however, whether temperatures would be high enough and radiative cooling would be slow enough to explain the discrepancy. Lastly, the total fragment abundances roughly correlate to the inverse values of D, however, no actual trend can be derived from the present data.

V. SUMMARY

Cationic and anionic molecules are produced from a heavily oxidized 232-thorium foil by laser ablation under high-vacuum conditions. Precision mass analysis is performed with a multireflection time-of-flight (MR-ToF) mass spectrometer. A number of contaminants including halogens as well as natural uranium are identified. Thorium is predominantly found in the form of oxides $\mathrm{Th}_n\mathrm{O}_x$ due to the advanced oxidation of the target foil. There is a strong preference to form $\mathrm{Th}_n\mathrm{O}_{2n-1}^+$ oxides, which might be linked to a production mechanism based on assembly from neutral ThO_2. The thorium-uranium compound ThUO_2^+ is the only observed molecule incorporating both actinides.

Photoexcitation measurements at $\lambda = 532$ nm show a preference to form thorium monomers Th^+ and monomer-based species ThX^+ from dimer-based species $\mathrm{Th}_2\mathrm{X}^+$. For the anionic species Th^-, ThO^-, and ThO_2^- only electron detachment is observed. The findings are supported by results from density functional theory yielding geometric structures and dissociation energies. Instead of thorium-thorium bonds, ground-state isomers show a preference for bridge-type bonds incorporating carbon, nitrogen, or oxygen.

ACKNOWLEDGMENTS

P.F. and L.S. acknowledge funding from the German Ministry for Education and Research (BMBF) under Grant No. 05P18HGCIA. J.S. acknowledges funding from the German Research Foundation (DFG) under Project No. 495729045. Ch.T. was supported by the Research Council of Norway through its Centres of Excellence scheme (Grant No. 262695), through the FRIPRO grant ReMRChem (Grant No. 324590), and NOTUR, the Norwegian Metacenter for Computational Science through grant of computer time (Grant No. nn14654k). We thank V. Pershina for initiating contact with Ch.T.

Author responsibilities: P.F., conceptualization, formal analysis, investigation (experimental), writing of original draft; J.S. resources, writing (review and editing); Ch.E.D., resources, supervision, writing (review and editing); D.R., resources, writing (review and editing); L.S., conceptualization, funding acquisition, supervision, writing (review and editing); Ch.T.: investigation (theoretical), writing (review and editing).

APPENDIX A: ION IDENTIFICATION VIA PRECISION MASS MEASUREMENTS

Selected species are stored in the MR-ToF analyzer for up to $N = 1000$ revolutions. The ion masses determined according to Eq. (1) are given in Table III. A high-abundance reference species marked "REFERENCE" is chosen for each mass range. The uncertainties of the calculated masses follow from those of the periods T and T_{ref}. Due to the investigations being performed over multiple days, systematic drifts in, e.g., applied voltages or ambient temperature lead to period fluctuations. Even though references are regularly remeasured, the large number of molecules and wide mass ranges still incur accuracy reductions. Thus, a systematic relative uncertainty of 3×10^{-6} is quadratically added to the statistical one. This value is chosen based on the observed period drifts over the course of multiple days. Note that the performance of the mass measurements is slightly worse in the topmost block of Table III. This is due to larger relative mass differences between the references and ions of interest as well as the MR-ToF analyzer producing worse signal shapes since it is optimized for larger masses in this study.

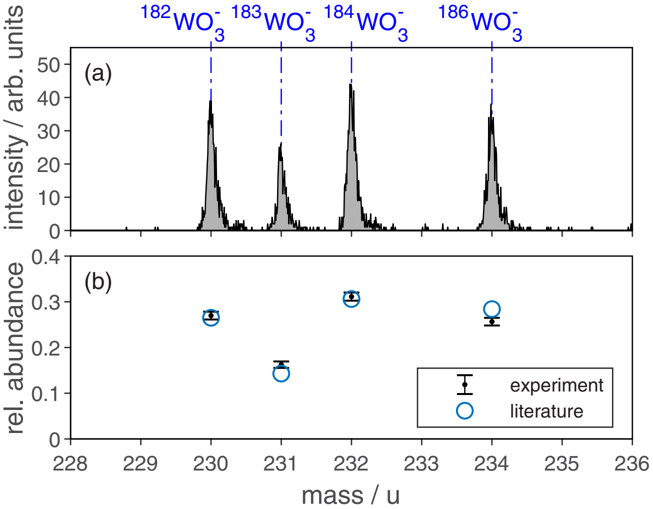

FIG. 11. (a) Spectrum of anionic signals around $A = 232$ from new laser-ablation spot. (b) Relative abundance of recorded signals (black) and natural abundance distribution of tungsten isotopes (blue) [68].

APPENDIX B: MOLECULES NOT CONTAINING THORIUM

Next to the molecules discussed in the main text, there is an unknown cationic signal at $A = 156$ as well as an anionic signal at $A = 175$. The determined mass of the cation matches that of $^{137}\mathrm{Ba}\,^{19}\mathrm{F}^+$ which might be explained by the age of the target foil. However, the isotope distribution of the neighboring mass numbers does not match that of barium. Specifically, the most-abundant natural isotope $^{138}\mathrm{Ba}$ should lead to a significantly higher signal on $A = 157$ which is not observed.

Isotope distributions are an important tool for element identification. For example, the distribution of WO_3^- anions between $A = 230$ and 234 found on new laser-ablation spots (Fig. 11) matches the natural abundances of tungsten isotopes. This both confirms the molecule and highlights that no significant amount of thorium is present on $A = 232$. The anionic species on mass numbers $A = 26$ and 27 are identified similarly: While the determined mass of $^{10}\mathrm{B}\,^{16}\mathrm{O}^-$ only fits its expected value within two standard deviations, the relative abundance of $^{10}\mathrm{B}$ and $^{11}\mathrm{B}$ confirms the molecule.

[1] R. F. Gacia Ruiz, R. Berger, J. Billowes, C. L. Binnersley, M. L. Bissell, A. A. Breier, A. J. Brinson, K. Chrysalidis, T. E. Cocolios, B. S. Cooper, K. T. Flanagan, T. F. Giesen, R. P. de Groote, S. Franchoo, F. P. Gustafsson, T. A. Isaev, A. Koszorús, G. Neyens, H. A. Perrett, C. M. Ricketts *et al.*, Spectroscopy of short-lived radioactive molecules, Nature (London) **581**, 396 (2020).

[2] S. M. Udrescu, A. J. Brinson, R. F. G. Ruiz, K. Gaul, R. Berger, J. Billowes, C. L. Binnersley, M. L. Bissell, A. A. Breier, K. Chrysalidis, T. E. Cocolios, B. S. Cooper, K. T. Flanagan, T. F. Giesen, R. P. de Groote, S. Franchoo, F. P. Gustafsson, T. A. Isaev, A. Koszorús, G. Neyens *et al.*, Isotope shifts of radium monofluoride molecules, Phys. Rev. Lett. **127**, 033001 (2021).

[3] G. Arrowsmith-Kron, M. Athanasakis-Kaklamanakis, M. Au, J. Ballof, R. Berger, A. Borschevsky, A. A. Breier, F. Buchinger, D. Budker, L. Caldwell, C. Charles, N. Dattani, R. P. de Groote, D. DeMille, T. Dickel, J. Dobaczewski, C. E. Düllmann, E. Eliav, J. Engel, M. Fan *et al.*, Opportunities for fundamental physics research with radioactive molecules, Rep. Prog. Phys. **87**, 084301 (2024).

[4] J. Ballof, N. Nusgart, P. Lalain, M. Au, R. Heinke, D. Leimbach, S. Stegemann, M. Schütt, S. Rothe, and J. T. Singh, Progress towards the FRIB-EDM^3-Frontend: A tool to provide radioactive molecules from isotope harvesting for fundamental symmetry studies, Nucl. Instrum. Methods Phys. Res. Sect. B **541**, 224 (2023).

[5] L. Landau, On the conservation laws for weak interactions, Nucl. Phys. **3**, 127 (1957).

[6] L. V. Skripnikov, N. S. Mosyagin, A. V. Titov, and V. V. Flambaum, Actinide and lanthanide molecules to search for strong CP-violation, Phys. Chem. Chem. Phys. **22**, 18374 (2020).

[7] M. Fan, C. A. Holliman, X. Shi, H. Zhang, M. W. Straus, X. Li, S. W. Buechele, and A. M. Jayich, Optical mass spectrometry of cold $RaOH^+$ and ${RaOCH_3}^+$, Phys. Rev. Lett. **126**, 023002 (2021).

[8] P. Yu and N. R. Hutzler, Probing fundamental symmetries of deformed nuclei in symmetric top molecules, Phys. Rev. Lett. **126**, 023003 (2021).

[9] V. Andreev, D. G. Ang, D. DeMille, J. M. Doyle, G. Gabrielse, J. Haefner, N. R. Hutzler, Z. Lasner, C. Meisenhelder, B. R. O'Leary, C. D. Panda, A. D. West, E. P. West, and X. Wu, Improved limit on the electric dipole moment of the electron, Nature (London) **562**, 355 (2018).

[10] C. R. J. Charles, F. Ames, O. Kester, S. Malbrunot-Ettenauer, C. Babcock, B. E. Schultz, C. Peters, E. L. Flannigan, J.-F. Alary, A. Laxdal, P. Kunz, J. Lassen, A. Teigelhoefer, P. J. A. McCausland, and R. Flemming, Production of radioactive molecular ions in radiofrequency quadrupole gas-reaction cells, J. Phys.: Conf. Ser. **2244**, 012100 (2022).

[11] M. Au, M. Athanasakis-Kaklamanakis, L. Nies, J. Ballof, R. Berger, K. Chrysalidis, P. Fischer, R. Heinke, J. Johnson, U. Köster, D. Leimbach, B. Marsh, M. Mougeot, B. Reich, J. Reilly, E. Reis, M. Schlaich, C. Schweiger, L. Schweikhard, S. Stegemann *et al.*, In-source and in-trap formation of molecular ions in the actinide mass range at CERN-ISOLDE, Nucl. Instrum. Methods Phys. Res. Sect. B **541**, 375 (2023).

[12] M. Au, L. Nies, S. Stegemann, M. Athanasakis-Kaklamanakis, T. E. Cocolios, P. Fischer, P. F. Giesel, J. D. Johnson, U. Köster, D. Lange, M. Mougeot, J. Reilly, M. Schlaich, C. Schweiger, L. Schweikhard, F. Wienholtz, W. Wojtaczka, Ch. E. Düllmann, and S. Rothe, Production and purification of molecular ^{225}Ac at CERN-ISOLDE, J. Radioanal. Nucl. Chem. (2024).

[13] J. Marçalo, J. P. Leal, and A. P. de Matos, Gas phase actinide ion chemistry: Activation of alkanes and alkenes by thorium cations, Int. J. Mass Spectrom. Ion Processes **157-158**, 265 (1996).

[14] H. H. Cornehl, R. Wesendrup, M. Diefenbach, and H. Schwarz, A comparative study of oxo-ligand effects in the gas-phase chemistry of atomic lanthanide and actinide cations, Chem. Eur. J. **3**, 1083 (1997).

[15] R. Johnsen, F. R. Castell, and M. A. Biondi, Rate coefficients for oxidation of Ti^+ and Th^+ by O_2 and NO at low energies, J. Chem. Phys. **61**, 5404 (1974).

[16] C. C. L. Pereira, R. Maurice, A. F. Lucena, S. Hu, A. P. Gonçalves, J. Marçalo, J. K. Gibson, L. Andrews, and L. Gagliardi, Thorium and uranium carbide cluster cations in the gas phase: Similarities and differences between thorium and uranium, Inorg. Chem. **52**, 10968 (2013).

[17] R. M. Cox, P. B. Armentrout, and W. A. de Jong, Activation of CH_4 by Th^+ as studied by guided ion beam mass spectrometry and quantum chemistry, Inorg. Chem. **54**, 3584 (2015).

[18] J. K. Gibson, Gas-phase chemistry of actinide ions: probing the distinctive character of the 5f elements, Int. J. Mass Spectrom. **214**, 1 (2002).

[19] L. Kroger and C. Reich, Features of the low-energy level scheme of ^{229}Th as observed in the α-decay of ^{223}U, Nucl. Phys. A **259**, 29 (1976).

[20] E. Peik and M. Okhapkin, Nuclear clocks based on resonant excitation of γ-transitions, C. R. Phys. **16**, 516 (2015).

[21] S. Kraemer, J. Moens, M. Athanasakis-Kaklamanakis, S. Bara, K. Beeks, P. Chhetri, K. Chrysalidis, A. Claessens, T. Cocolios, J. G. M. Correia, H. Witte, R. Ferrer, S. Geldhof, R. Heinke, N. Hosseini, M. Huyse, U. Köster, Y. Kudryavtsev, M. Laatiaoui, R. Lica *et al.*, Observation of the radiative decay of the ^{229}Th nuclear clock isomer, Nature (London) **617**, 706 (2023).

[22] J. Tiedau, M. V. Okhapkin, K. Zhang, J. Thielking, G. Zitzer, E. Peik, F. Schaden, T. Pronebner, I. Morawetz, L. T. De Col, F. Schneider, A. Leitner, M. Pressler, G. A. Kazakov, K. Beeks, T. Sikorsky, and T. Schumm, Laser excitation of the Th-229 nucleus, Phys. Rev. Lett. **132**, 182501 (2024).

[23] V. V. Flambaum, Enhanced nuclear schiff moment and time-reversal violation in ^{229}Th-containing molecules, Phys. Rev. C **99**, 035501 (2019).

[24] P. F. Giesel, P. Fischer, and L. Schweikhard, A multi-reflection time-of-flight setup for the study of atomic clusters produced by magnetron sputtering, Rev. Sci. Instrum. **95**, 023201 (2024).

[25] R. N. Wolf, G. Marx, M. Rosenbusch, and L. Schweikhard, Static-mirror ion capture and time focusing for electrostatic ion-beam traps and multi-reflection time-of-flight mass analyzers by use of an in-trap potential lift, Int. J. Mass Spectrom. **313**, 8 (2012).

[26] P. Fischer and L. Schweikhard, Multiple active voltage stabilizations for multi-reflection time-of-flight mass spectrometry, Rev. Sci. Instrum. **92**, 063203 (2021).

[27] P. Fischer, S. Knauer, G. Marx, and L. Schweikhard, In-depth study of in-trap high-resolution mass separation by transversal

ion ejection from a multi-reflection time-of-flight device, Rev. Sci. Instrum. **89**, 015114 (2018).

[28] S. Knauer, P. Fischer, G. Marx, B. Schabinger, L. Schweikhard, and R. N. Wolf, Multi-reflection time-of-flight mass spectrometry with combined in-trap lift capture and mirror-switch ejection, Int. J. Mass Spectrom. **423**, 46 (2017).

[29] Y. Ito, P. Schury, M. Wada, S. Naimi, T. Sonoda, H. Mita, F. Arai, A. Takamine, K. Okada, A. Ozawa, and H. Wollnik, Single-reference high-precision mass measurement with a multireflection time-of-flight mass spectrograph, Phys. Rev. C **88**, 011306(R) (2013).

[30] S. Kimura, Y. Ito, D. Kaji, P. Schury, M. Wada, H. Haba, T. Hashimoto, Y. Hirayama, M. MacCormick, H. Miyatake, J. Moon, K. Morimoto, M. Mukai, I. Murray, A. Ozawa, M. Rosenbusch, H. Schatz, A. Takamine, T. Tanaka, Y. Watanabe *et al.*, Atomic masses of intermediate-mass neutron-deficient nuclei with relative uncertainty down to 35-ppb via multireflection time-of-flight mass spectrograph, Int. J. Mass Spectrom. **430**, 134 (2018).

[31] P. Fischer and L. Schweikhard, Multiple-ion-ejection multi-reflection time-of-flight mass spectrometry for single-reference mass measurements with lapping ion species, Rev. Sci. Instrum. **91**, 023201 (2020).

[32] P. Fischer and L. Schweikhard, Photofragmentation of Bi_n+/- clusters (n = 2-19) in an electrostatic ion beam trap, Eur. Phys. J. D **73**, 105 (2019).

[33] P. Fischer, P. Giesel, and L. Schweikhard, Photodissociation of small group-14 atomic clusters in a multi-reflection time-of-flight mass spectrometer, Eur. Phys. J. D **77**, 27 (2023).

[34] P. Fischer and L. Schweikhard, Isotope-resolved photodissociation pathways of lead-doped bismuth clusters from tandem multi-reflection time-of-flight mass spectrometry, Phys. Rev. Res. **1**, 033050 (2019).

[35] V. Blum, R. Gehrke, F. Hanke, P. Havu, V. Havu, X. Ren, K. Reuter, and M. Scheffler, *Ab initio* molecular simulations with numeric atom-centered orbitals, Comput. Phys. Commun. **180**, 2175 (2009).

[36] C. Lessig, T. de Witt, and E. Fiume, Efficient and accurate rotation of finite spherical harmonics expansions, J. Comput. Phys. **231**, 243 (2012).

[37] W. P. Huhn and V. Blum, One-hundred-three compound band-structure benchmark of post-self-consistent spin-orbit coupling treatments in density functional theory, Phys. Rev. Mater. **1**, 033803 (2017).

[38] C. van Wüllen, Molecular density functional calculations in the regular relativistic approximation: Method, application to coinage metal diatomics, hydrides, fluorides and chlorides, and comparison with first-order relativistic calculations, J. Chem. Phys. **109**, 392 (1998).

[39] J. van Lenthe, S. Faas, and J. Snijders, Gradients in the *ab initio* scalar zeroth-order regular approximation (ZORA) approach, Chem. Phys. Lett. **328**, 107 (2000).

[40] J. P. Perdew, K. Burke, and M. Ernzerhof, Generalized gradient approximation made simple, Phys. Rev. Lett. **77**, 3865 (1996).

[41] See Supplemental Material at http://link.aps.org/supplemental/10.1103/PhysRevResearch.6.043317 for total energies and XYZ-coordinates of calculated structures as well as orbital data for elements used in the calculation.

[42] C. J. Campbell, A. V. Steele, L. R. Churchill, M. V. DePalatis, D. E. Naylor, D. N. Matsukevich, A. Kuzmich, and M. S. Chapman, Multiply charged thorium crystals for nuclear laser spectroscopy, Phys. Rev. Lett. **102**, 233004 (2009).

[43] K. Zimmermann, M. V. Okhapkin, O. A. Herrera-Sancho, and E. Peik, Laser ablation loading of a radiofrequency ion trap, Appl. Phys. B **107**, 883 (2012).

[44] M. Piotrowski, J. Scarabel, M. Lobino, E. Streed, and S. Gensemer, Studies of thorium and ytterbium ion trap loading from laser ablation for gravity monitoring with nuclear clocks, OSA Continuum **3**, 2210 (2020).

[45] R. M. Cox, M. Citir, P. B. Armentrout, S. R. Battey, and K. A. Peterson, Bond energies of ThO^+ and ThC^+: A guided ion beam and quantum chemical investigation of the reactions of thorium cation with O_2 and CO, J. Chem. Phys. **144**, 184309 (2016).

[46] G. G. Briggs and J. H. Cavendish, Thorium metal production, in *AIME Centennial Meeting* (National Lead Company of Ohio, Cincinnati, Ohio, 1971).

[47] Y. Li, J. Zou, X.-G. Xiong, H. Xie, Z. Tang, M. Ge, Y. Zhao, and H. Liu, Anion photoelectron spectroscopy and chemical bonding of ThO_2^- and ThO_3, J. Chem. Phys. **148**, 244304 (2018).

[48] E. G. Rauh and R. J. Ackermann, First ionization potentials of some refractory oxide vapors, J. Chem. Phys. **60**, 1396 (1974).

[49] T. Steimle, D. L. Kokkin, S. Muscarella, and T. Ma, Detection of the thorium dimer via two-dimensional fluorescence spectroscopy, J. Phys. Chem. A **119**, 9281 (2015).

[50] Z. Zhu, M. Marshall, R. M. Harris, K. H. Bowen, M. Vasiliu, and D. A. Dixon, Th_2O^-, Th_2Au^-, and $Th_2AuO_{1,2}^-$ Anions: Photoelectron spectroscopic and computational characterization of energetics and bonding, J. Phys. Chem. A **125**, 258 (2021).

[51] M. C. Heaven, Probing actinide electronic structure using fluorescence and multi-photon ionization spectroscopy, Phys. Chem. Chem. Phys. **8**, 4497 (2006).

[52] J. Han, L. A. Kaledin, V. Goncharov, A. V. Komissarov, and M. C. Heaven, Accurate ionization potentials for UO and UO_2: A rigorous test of relativistic quantum chemistry calculations, J. Am. Chem. Soc. **125**, 7176 (2003).

[53] K. H. Lau, R. D. Brittain, and D. L. Hildenbrand, High temperature thermodynamic studies of some gaseous thorium fluorides, J. Chem. Phys. **90**, 1158 (1989).

[54] P. Fischer and L. Schweikhard, Decay-rate power-law exponent as a link between dissociation energy and temperature, Phys. Rev. Res. **2**, 043177 (2020).

[55] G. Cavigliasso and N. Kaltsoyannis, On the paucity of molecular actinide complexes with unsupported metal-metal bonds: A comparative investigation of the electronic structure and metal-metal bonding in U_2X_6 (X = Cl, F, OH, NH_2, CH_3) Complexes and d-Block Analogues, Inorg. Chem. **45**, 6828 (2006).

[56] S. Knecht, H. J. A. Jensen, and T. Saue, Relativistic quantum chemical calculations show that the uranium molecule U_2 has a quadruple bond, Nat. Chem. **11**, 40 (2019).

[57] L. N. Gorokhov, A. M. Emelyanov, and Y. S. Khodeev, Mass-spectroscopic investigation of stability of gaseous molecules of U_2O_2 and U_2, High Temp. **12**, 1156 (1974).

[58] J. T. Boronski, J. A. Seed, D. Hunger, A. W. Woodward, J. van Slageren, A. J. Wooles, L. S. Natrajan, N. Kaltsoyannis, and S. T. Liddle, A crystalline tri-thorium cluster with σ-aromatic metal-metal bonding, Nature (London) **598**, 72 (2021).

[59] X. Zhang, Y. Wang, R. Morales-Martínez, J. Zhong, C. de Graaf, A. Rodríguez-Fortea, J. M. Poblet, L. Echegoyen, L. Feng, and N. Chen, $U_2@I_h(7)$-C_80: Crystallographic characterization of a long-sought dimetallic actinide endohedral fullerene, J. Am. Chem. Soc. **140**, 3907 (2018).

[60] P. Popelier, F. Aicken, and S. O'Brien, Atoms in molecules, *Chemical Modelling: Applications and Theory, Volume 1* (The Royal Society of Chemistry, London, 2000), Chap. 3, p. 143.

[61] A. O. de-la Roza, M. Blanco, A. M. Pendás, and V. L. na, Critic: a new program for the topological analysis of solid-state electron densities, Comput. Phys. Commun. **180**, 157 (2009).

[62] A. O. de-la Roza, E. R. Johnson, and V. Luaña na, CRITIC2: A program for real-space analysis of quantum chemical interactions in solids, Comput. Phys. Commun. **185**, 1007 (2014).

[63] C. Gatti and P. Macchi, A guided tour through modern charge density analysis, in *Modern Charge-Density Analysis*, edited by C. Gatti and P. Macchi (Springer, Dordrecht, 2012), pp. 1–78.

[64] C. Tantardini, E. V. Boldyreva, and E. Benassi, Hypervalency in organic crystals: A case study of the oxicam sulfonamide group, J. Phys. Chem. A **120**, 10289 (2016).

[65] C. Tantardini and A. Michalchuk, Dess-martin periodinane: The reactivity of a λ^5-iodane catalyst explained by topological analysis, Int. J. Quantum Chem. **119**, e25838 (2019).

[66] R. S. Stepanov, A. D. Radina, C. Tantardini, A. G. Kvashnin, and A. V. Kolobov, Chemical bonding within AIIIBVI materials under uniaxial compression, Phys. Chem. Chem. Phys. **26**, 20984 (2024).

[67] M. Wang, W. J. Huang, F. G. Kondev, G. Audi, and S. Naimi, The AME 2020 atomic mass evaluation (II). Tables, graphs and references, Chinese Phys. C **45**, 030003 (2021).

[68] J. Meija, T. B. Coplen, M. Berglund, W. A. Brand, P. D. Bièvre, M. Gröning, N. E. Holden, J. Irrgeher, R. D. Loss, T. Walczyk, and T. Prohaska, Isotopic compositions of the elements 2013 (IUPAC Technical Report), Pure Appl. Chem. **88**, 293 (2016).